ORIGINAL PAPER

Quantifying dithiothreitol displacement of functional ligands from gold nanoparticles

De-Hao Tsai · Melanie P. Shelton · Frank W. DelRio ·
Sherrie Elzey · Suvajyoti Guha · Michael R. Zachariah ·
Vincent A. Hackley

Abstract Dithiothreitol (DTT)-based displacement is widely utilized for separating ligands from their gold nanoparticle (AuNP) conjugates, a critical step for differentiating and quantifying surface-bound functional ligands and therefore the effective surface density of these species on nanoparticle-based therapeutics and other functional constructs. The underlying assumption is that DTT is smaller and much more reactive toward gold compared with most ligands of interest, and as a result will reactively displace the ligands from surface sites thereby enabling their quantification. In this study, we use complementary dimensional and spectroscopic methods to characterize the efficiency of DTT displacement. Thiolated methoxypolyethylene glycol (SH-PEG) and bovine serum albumin (BSA) were chosen as representative ligands. Results clearly show that (1) DTT does not completely displace bound SH-PEG or BSA from AuNPs, and (2) the displacement efficiency is dependent on the binding affinity between the ligands and the AuNP surface. Additionally, the displacement efficiency for conjugated SH-PEG is moderately dependent on the molecular mass (yielding efficiencies ranging from 60 to 80 % measured by ATR-FTIR and ≈90 % by ES-DMA), indicating that the displacement efficiency for SH-PEG is predominantly determined by the S–Au bond. BSA is particularly difficult to displace with DTT (i.e., the displacement efficiency is nearly zero) when it is in the so-called normal form. The displacement efficiency for BSA improves to 80 % when it undergoes a conformational change to the expanded form through a process of pH change or treatment with a surfactant. An analysis of the three-component system (SH-PEG+BSA+AuNP) indicates that the presence of SH-PEG decreases the displacement efficiency for BSA, whereas the displacement efficiency for SH-PEG is less impacted by the presence of BSA.

D.-H. Tsai · M. P. Shelton · F. W. DelRio · S. Elzey · S. Guha ·
M. R. Zachariah · V. A. Hackley (✉)
Material Measurement Laboratory,
National Institute of Standards and Technology,
Gaithersburg, MD 20899, USA
e-mail: vince.hackley@nist.gov

S. Guha · M. R. Zachariah
Departments of Mechanical Engineering and Chemistry,
University of Maryland,
College Park, MD 20740, USA

Present Address:
S. Elzey
TSI Incorporated,
500 Cardigan Road,
Shoreview, MN 55126, USA

Introduction

Gold nanoparticles (AuNPs) are attractive for a variety of emerging biomedical applications (e.g., therapeutics and diagnostics) [1–15]. In addition to biocompatibility, AuNPs have the advantageous property of tunable surface plasmon resonance absorption, an effect that can be exploited in applications such as imaging, optical-based molecular detection, and hyperthermal treatment [16–18]. In addition, the thiol-Au surface chemistry provides an effective route for the design and attachment of functional molecular structures. For example, AuNPs can be used to achieve targeted cell-specific uptake for efficient gene therapy [7, 8, 16], and cancer

treatments based on AuNP platforms have undergone clinical testing [19, 20]. In this respect, citrate-stabilized AuNPs have frequently been utilized as a precursor for ligation with functional thiolated molecular species; weakly bound citrate is easily displaced by the covalently bound thiol [2].

The surface density and relative distributions of bound ligands are critical from a pharmacological perspective and directly influence both performance and absorption–distribution–metabolism–excretion properties [5, 21]. A current limitation of nanotechnology-based therapeutics is that methods for conjugating AuNPs with functional ligands generally do not provide quantitative control of adsorption density, particularly when multiple ligand species are involved. From the viewpoints of efficacy and safety, it is therefore desirable to develop effective measurement methods to characterize these ligands in the bound state, including quantitative information on molecular packing density, which can be used to determine and control a delivered therapeutic dose. In addition, affinity parameters such as equilibrium binding and desorption constants for ligands are useful in formulation design since they can be correlated to conjugate stability [11, 13, 14].

Detach-and-analyze methodology is a common approach to study molecular conjugation and to quantify the number of molecules bound to the surface of AuNPs (i.e., the surface packing density). The general concept is to detach ligands from the surface and remove the particle phase (e.g., by centrifugation) prior to analysis, and then to directly measure the concentration of ligands in solution using available analytical tools (e.g., optical absorption, fluorescence, or mass spectrometry). A clear advantage of this approach is the capacity to quantify multiple species of ligands simultaneously without interference from the particle phase. Additionally, the analytical methods used to measure free ligands in solution are well developed and validated, relative to approaches used in nanoparticle metrology [8, 11, 13, 15].

In order to analytically quantify molecular conjugation using detach-and-analyze methodology, it is necessary to have near 100 % efficiency of detachment (or a measurable and predictable efficiency that is sufficiently high to yield reasonable sensitivity and precision). This requires application of a suitable chemical reagent, such as dithiothreitol (DTT, $C_4H_{10}O_2S_2$), which is widely used for AuNP-based platforms [1–4, 22]. The assumptions are that (1) DTT is small and compact, and should therefore more easily penetrate surface corona to reach the AuNP surface, and (2) with two thiol groups, DTT has a high affinity for the Au surface [23, 24], and, if added in excess, should completely displace most ligands of interest.

Though promising in concept, the efficiency of ligand displacement by DTT is not always clearly demonstrated and is infrequently reported. Additionally, the assumption that DTT displacement is equally efficient for different ligands, especially in a mixed-ligand conjugate, as we will demonstrate, is not sound. The potential incomplete displacement of functional ligands could result in a deviation of the resulting accuracy (e.g., surface packing density), yielding misleading information on therapeutic dose.

The objective of this study was simple: to quantify the detachment efficiency of DTT for model conjugated AuNPs using multiple characterization methods. Thiolated methoxy-polyethylene glycol (SH-PEG) and bovine serum albumin (BSA) were used as representative ligands due to their importance in nanomedicine. BSA is homologous to human serum albumin and serves as a representative serum protein in the context of this work [13]. PEG is used to create a functional hydrophilic coating to reduce serum protein adsorption and to protect AuNP-based therapeutics from rapid clearance by the reticuloendothelial system, thus increasing the circulation time in the bloodstream [1, 4, 5, 7, 11, 25]. Dynamic light scattering (DLS) and electrospray differential mobility analysis (ES-DMA) are utilized to provide dimensional metrics for conjugated AuNPs under wet and dry states, respectively [8, 11, 13, 14]. With attenuated total reflectance–Fourier transform infrared (ATR-FTIR) spectroscopy and inductively coupled plasma–mass spectroscopy (ICP-MS), we can exploit characteristic absorption and mass signals, respectively, corresponding to specific ligands conjugated to the AuNPs [13–15]. Our approach is to obtain the displacement efficiency, by which we can effectively improve the accuracy of molecular conjugation analysis [as depicted in the Electronic supplementary material (ESM)].

Experimental methods

Materials

Commercially available 60-nm citrate-stabilized monodisperse colloidal AuNPs were obtained from Ted Pella Inc. (Redding, CA) [26]. The as-received number concentration of AuNPs in solution was $\approx 2.6 \times 10^{10} cm^{-3}$. Aqueous DTT (99 %, Sigma-Aldrich, St. Louis, MO) was freshly prepared on the day of use, and the concentration of DTT (C_{DTT}) ranged from 0.016 to 942 mmol/L. Sodium dodecyl sulfate (SDS, 99 %, Alfa Aesar, Ward Hill, MA) was prepared at a concentration (denoted as C_{SDS}) of 35 mmol/L. From Nanocs (New York, NY), we obtained 1 kDa SH-PEG (SH-PEG1K), 10 kDa SH-PEG (SH-PEG10K), and 20 kDa SH-PEG (SH-PEG20K). From JenKem Technology (Allen, TX), we obtained 5 kDa SH-PEG (SH-PEG5K). In all cases, SH-PEG was used without further purification, but diluted to concentrations ranging from C_{SH-PEG}=0.1 to 1 mmol/L. Highly purified reagent-grade BSA (≥98 % protein, ≤3 endotoxin units/mg, fatty acid- and IgG-free, SeraCare Life Science, Milford, MA) was utilized at concentrations ranging from

C_{BSA}=2 to 100 µmol/L. In both cases (SH-PEG and BSA), the concentration range exceeds the saturation concentrations determined in previous work [11, 13, 14]. To prepare SH-PEG or BSA-conjugated AuNPs, 200 µL of a SH-PEG (1 mmol/L) or BSA (500 µmol/L) aqueous solution was first prepared, then mixed with 800 µL of AuNPs and incubated overnight. The ligand to AuNP number ratio was 4.6×10^6 and 2.3×10^6 for SH-PEG and BSA, respectively. Based on our previous research [13, 14], these large excesses should be sufficient to achieve surface saturation. Aqueous ammonium acetate (99.9 %, Sigma-Aldrich) solution was prepared and used to adjust ionic strength ($\approx$2.5 mmol/L, 0.03 S/m). The pH was measured using an Orion 3 STAR meter (Thermo Electron, Madison, WI) with an InLab semi-micro glass electrode (Mettler, Toledo, MI). Biological grade 18.2 MΩ cm deionized (DI) water (Aqua Solutions, Jasper, GA) was used for preparing solutions and AuNP suspensions.

DLS and ES-DMA

DLS measurements were performed using a Zetasizer Nano (Malvern Instruments, Westborough, MA). The ES-DMA system consists of an electrospray aerosol generator (Model 3480, TSI Inc., Shoreview, MN), a differential mobility analyzer (DMA, Model 3080n, TSI Inc., Shoreview, MN), and a condensation particle counter (Model 3025, TSI Inc., Shoreview, MN). Details of the DLS and ES-DMA experimental setups and analysis have been described in previous publications [6, 8, 11, 27, 28] and are also summarized in the ESM.

ATR-FTIR

ATR-FTIR spectroscopy was performed using a Nicolet Spectra 750 FTIR spectrometer equipped with a Thunder Dome ATR accessory using either a germanium or a diamond crystal flat (Thermo Scientific, Madison, WI). Spectra were collected from an average of 128 scans with a resolution of 1 cm^{-1}. Details of sample preparation, experimental procedures, and data analysis are described in the ESM. For clarity, results from the Ge-ATR accessory are principally reported in the main text and complementary results from the diamond ATR, unless otherwise noted, are presented in the ESM.

ICP-MS

An ICP-MS (Model 7700, Agilent, Santa Clara, CA) was used to measure the mass fraction of Au and S using calibration curves generated from standard solutions. Details of sample preparation and measurement conditions are described in our previous publication [29] and summarized in the ESM.

Measurement uncertainty

Error bars shown in figures and uncertainty ranges associated with measurement values represent one standard deviation calculated from replicate (two to four) measurements performed under repeatability conditions.
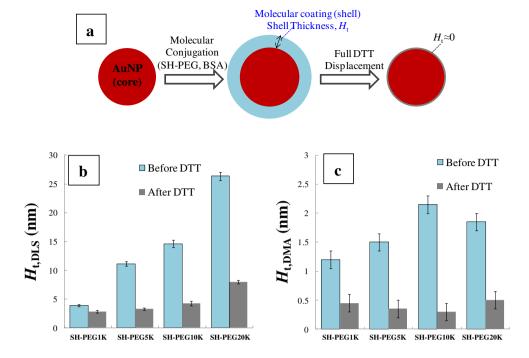
Results and discussion

SH-PEG-conjugated AuNPs

DLS is used to measure the spherical equivalent hydrodynamic diameter, $d_{p,hz}$, of ligand-conjugated AuNPs, and thereby to monitor the change in hydrodynamic size, $\Delta d_{p,hz}$ ($=d_{p,hz}-d_{p0,hz}$, where $d_{p0,hz}$ is the diameter of the unconjugated citrate-stabilized AuNPs). Four different molecular masses, M_m, of SH-PEG were utilized in this study: 1, 5, 10, and 20 kDa. Using the core–shell model depicted in Fig. 1a, the thickness of the molecular corona ($H_{t,DLS}$) is related to the increase in particle size by $H_{t,DLS}=\Delta d_{p,hz}/2$. Because DTT is a small, compact molecule in comparison to the SH-PEG species used in the study, its affect on $H_{t,DLS}$ is small ($H_{t,DLS}\approx0.5$ nm for DTT-conjugated AuNPs) and typically within the statistical uncertainty of the measurements. Therefore, when DTT interacts with SH-PEG-conjugated AuNPs, a *reduction* in $H_{t,DLS}$ can be principally attributed to displacement of SH-PEG by DTT.

As shown in Fig. 1b, following conjugation with excess ligand, $H_{t,DLS}$ is observed to range from $\approx$4 to 26 nm, consistent with the formation of a PEG corona on the AuNPs. After treatment with DTT (incubation time was >3 h in all experiments), $H_{t,DLS}$ decreases significantly for all M_m, indicating desorption of SH-PEG from the AuNP surface. As shown in Fig. 1c, ES-DMA results also confirm that SH-PEG is displaced by DTT. For all M_m, the molecular corona thickness measured by ES-DMA, $H_{t,DMA}$ ($=\Delta d_{p,m}/2$), decreases with the addition of DTT. Here, $\Delta d_{p,m}$ is the change in mobility particle diameter ($\Delta d_{p,m}=d_{p,m}-d_{p0,m}$, where $d_{p,m}$ is the mobility diameter of AuNPs measured by DMA, and $d_{p0,m}$ is the $d_{p,m}$ of unconjugated citrate-stabilized AuNPs). For DTT-conjugated AuNPs, we found $d_{p,m}\approx d_{p0,m}$, similar to the result measured by DLS. Table 1 lists the values of $H_{t,DLS}$ and $H_{t,DMA}$ from Fig. 1b, c. The differences between $H_{t,DLS}$ and $H_{t,DMA}$ are mainly due to the different environmental conditions associated with each measurement (i.e., liquid phase in DLS and dry aerosol in ES-DMA), which has been discussed in more detail in previous work [11, 13, 15]. It is worth noting that post-DTT-treated samples were cleaned by centrifugation to remove unbound ligands prior to analysis by ES-DMA in order to avoid deposition of the ligands onto the aerosolized particles; however, this process was not performed prior to DLS analysis because the size of the ligands in solution is sufficiently

Fig. 1 Effect of DTT on displacement of SH-PEG-conjugated AuNPs measured by physical characterization methods. **a** Core–shell model for depicting the change in $H_{t,DLS}$ and $H_{t,DMA}$ after SH-PEG conjugation and the subsequent DTT displacement. **b** $H_{t,DLS}$ from DLS. **c** $H_{t,DMA}$ by ES-DMA. C_{DTT}=86 mmol/L and C_{SH-PEG}=200 µmol/L

small to have no significant impact on the measured particle size.

Despite the significant changes in $H_{t,DLS}$ and $H_{t,DMA}$ following DTT treatment, it is clear that the molecular corona thickness does not return to the value of DTT-conjugated AuNPs, indicating that incomplete displacement is observed for all SH-PEG-conjugated AuNPs investigated. Using a previously developed analytical model [6, 11, 14], the surface packing density of SH-PEG, σ_{SH-PEG} (in units of square nanometers), is calculated from the ES-DMA results as follows:

$$\sigma_{SH-PEG} = \frac{\left[\left(d_{p,m} + 2H_{t,DMA}\right)^2 - d_{p,m}{}^2\right]^2}{\left[2d_{p,m} <x^2>\right]^2}, \qquad (1)$$

Where $<x^2>^{0.5}$ is the random-walk radius of SH-PEG assuming freely jointed Gaussian chains (values of $<x^2>^{0.5}$

are given in Table 2) [6, 11]. The displacement efficiency R_{SH-PEG} was then determined using the relationship

$$R_{SH-PEG} = \frac{\sigma_{SH-PEG,max} - \sigma_{SH-PEG}}{\sigma_{SH-PEG,max}}, \qquad (2)$$

where $\sigma_{SH-PEG,max}$ is σ_{SH-PEG} prior to DTT displacement. As shown in Table 2, R_{SH-PEG} is relatively constant near 90 %, without a clear dependence on M_m.
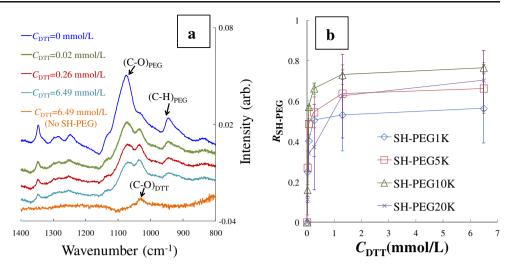
Flow cell ATR-FTIR was utilized in order to provide spectroscopic information on the DTT displacement process and to complement the size-based measurements. We used sequential injection for the flow cell ATR-FTIR measurements (i.e., starting from low C_{DTT} and proceeding to high C_{DTT}, followed by a DI water wash) [14], with a dwell time of 10 min at each step. Figure 2a shows the ATR-FTIR spectra for SH-PEG5K-conjugated AuNPs before and after DTT displacement; spectra for all other M_m are shown in the ESM. Prior to the addition of DTT (C_{DTT}=0, blue curve), two characteristic absorption bands representing SH-PEG5K adsorption on AuNPs were observed: 1,080 cm^{-1} due to C–O

Table 1 Summary of corona thickness measurements, $H_{t,DLS}$ and $H_{t,DMA}$, obtained from DLS and ES-DMA, respectively

Ligand	$H_{t,DLS}$ (nm)	$H_{t,DLS}$, after DTT (nm)	$H_{t,DMA}$ (nm)	$H_{t,DMA}$, after DTT (nm)
SH-PEG1K	3.9±0.2	2.8±0.3	1.2±0.2	0.4±0.2
SH-PEG5K	11.1±0.4	3.3±0.2	1.5±0.2	0.4±0.2
SH-PEG10K	14.6±0.7	4.3±0.4	2.2±0.2	0.7±0.2
SH-PEG20K	26.4±0.7	8.0±0.3	1.9±0.2	0.7±0.2

Table 2 Summary of $<x^2>^{0.5}$, R_{SH-PEG}, and $K_{d,SH-PEG}$ results from ES-DMA and ATR-FTIR

Ligand	$<x^2>^{0.5}$ (nm)	R_{SH-PEG} (%) by ES-DMA	R_{SH-PEG} (%) by ATR-FTIR	$K_{d,SH-PEG}$ (L/mol) by ATR-FTIR
SH-PEG1K	1.6	90±10	56±17	1.3×10^4
SH-PEG5K	3.7	92±5	66±12	1.5×10^4
SH-PEG10K	5.2	91±5	77±2	1.3×10^4
SH-PEG20K	7.3	86±6	70±15	0.5×10^4

Fig. 2 Effect of DTT on displacement of SH-PEG-conjugated AuNPs measured by flow-cell type ATR-FTIR. **a** ATR-FTIR spectra for SH-PEG5K-conjugated AuNPs before and after reaction with DTT; C_{DTT} ranging from 0 to 6.5 mmol/L; background subtracted spectrum is for unconjugated AuNPs in DI water. **b** Desorption isotherms for SH-PEG from AuNPs (by ATR-FTIR) as a function of C_{DTT}. Results are averages from measurements using both Ge and diamond flats. *Lines* are to guide the eyes

stretching (denoted as (C–O)$_{PEG}$) and 950 cm^{-1} due to C–H rocking (denoted as (C–H)$_{PEG}$) [30]. After adding DTT, the (C–O)$_{PEG}$ and (C–H)$_{PEG}$ peak intensities decreased, indicative of SH-PEG5K desorption from the AuNPs. Simultaneously, we noted the appearance of a peak at 1,030 cm^{-1}, which was attributed to the C–O stretching of DTT molecules adsorbed on AuNPs (denoted as (C–O)$_{DTT}$) [30]. These results confirm the DTT ligand displacement of SH-PEG from the conjugated AuNPs previously observed using dimensional methods (as shown in Fig. 1b, c). As C_{DTT} increases, the intensity of the (C–O)$_{DTT}$ peak increases and the intensities of the (C–O)$_{PEG}$ and (C–H)$_{PEG}$ peaks decrease, showing that SH-PEG5K desorption is directly related to the adsorption of DTT on the AuNP surface.

Using the ATR-FTIR results, R_{SH-PEG} is calculated as a function of C_{DTT} and M_m. The (C–H)$_{PEG}$ band is used to quantify σ_{SH-PEG} and the corresponding values for R_{SH-PEG}. The advantage is that the (C–H)$_{PEG}$ band is distinguishable from the characteristic bands of DTT; it may be possible to improve quantification by application of chemometric analysis [31], but the present work demonstrates proof of principle. As depicted in Fig. 2b (results are averaged from measurements using both Ge and diamond flats), R_{SH-PEG} increases as C_{DTT} increases at small C_{DTT}, but R_{SH-PEG} eventually reaches a maximum value between 0.6 and 0.8 when C_{DTT} >1.2 mmol/L. As a result, ATR-FTIR results show that about 20 to 40 % of conjugated SH-PEG remains on the AuNPs after treatment with DTT, confirming that DTT cannot entirely displace SH-PEG. In addition, the results show that R_{SH-PEG} is not strongly dependent on M_m. It is important to note that the R_{SH-PEG} values determined using ES-DMA are about 20 % larger than those obtained from ATR-FTIR; these variations can be attributed to differences in the measurement physics and uncertainty in the analytical models. From the prospect of the measurement physics, ATR-FTIR measures the DTT displacement efficiency within an immobilized AuNP film, which differs somewhat from the free particle

condition used in the size-based measurements. On the other hand, ES-DMA reflects the free particle (i.e., colloidal suspension) condition. However, selecting the correct molecular size is very important for DMA characterization, and this process may result in greater than 20 % variation in the calculated results [14]. A detailed discussion, including a comparison with ICP-MS, is described in the ESM.

Having plotted the ATR-FTIR-derived desorption isotherms, the desorption constants for SH-PEG, $K_{d,SH-PEG}$, from DTT displacement are calculated using the Langmuir desorption model; details regarding these calculations are given in the ESM. As shown in Table 2, $K_{d,SH-PEG} \approx 10^4$ L/mol for all M_m. The relatively large values for $K_{d,SH-PEG}$ are indicative of a strong displacing effect (i.e., R_{SH-PEG} reaches saturation at small values of C_{DTT}), despite the fact that DTT can not completely displace SH-PEG from the AuNPs.

Subsequently, the conformation of adsorbed DTT and the possible displacing mechanism were considered. As determined by ATR-FTIR and ICP-MS (in the absence of SH-PEG), the maximum surface packing density of DTT on the AuNP surface ($\sigma_{DTT,max}$) is about 4.0±0.3 and 5.1±0.2 nm^{-2}, respectively (adsorption isotherms for DTT are shown in the ESM). Even at large C_{DTT}, $\sigma_{DTT,max}$ is only about 62 to 78 % of the theoretical maximum density for a short-chain self-assembled monolayer (e.g., mercaptopropionic acid) [11, 29]. Hence, DTT likely forms a disordered layer on AuNPs: [23, 24] 62 to 78 % of DTT molecules having a single S–Au bond (upright attachment mode), with the remainder having two S–Au bonds (flat attachment mode). As many of the adsorbed DTT molecules contain a free thiol group, it is plausible that DTT continues to displace neighboring ligands (i.e., SH-PEG) until reaching an equilibrium state.

BSA-conjugated AuNPs

BSA was used as a prototypical serum protein to investigate DTT displacement efficiency for protein–AuNP conjugates.

As shown in Fig. 3a, two peaks characteristic of BSA adsorption are present in the ATR-FTIR spectra: the so-called Amide I band at 1,650 cm^{-1} and the Amide II band at 1,540 cm^{-1} [13, 14]. After introducing DTT at neutral pH, there is no observable change in the Amide I or Amide II bands. Thus, the BSA–AuNP conjugate appears very stable relative to the SH-PEG conjugates (Figs. 1 and 2), and the displacement efficiency is correspondingly low. The difference in displacement efficiency observed between BSA and SH-PEG could simply be due to higher affinity of BSA on Au. BSA has 17 disulfide linkages within its tertiary structure, and one free cysteine residue that can react with the AuNP surface [32]. Once adsorbed to the AuNP, the BSA structure may be denatured allowing the formation of additional S–Au bonds, thereby increasing binding affinity [13]. Moreover, other functional groups in the amino sequence of BSA, such as NH$_2$, can also bind with the AuNP surface to increase affinity. Finally, the molecular mass of BSA is more than 3× that of the largest SH-PEG ligand used

here, and this may contribute to greater stability on the surface.

The low displacement efficiency for BSA–AuNP conjugates could indicate a substantial concern for the quantification of surface packing density based on separating ligands from the particle using agents like DTT as a low ligand recovery rate limits measurement sensitivity. Clearly, variations in displacement efficiency between different types of ligands must be taken into consideration. In order to ensure the accuracy of the calculations, it is necessary to reduce the affinity between BSA and the AuNP surface. One possible method for reducing the affinity is by altering the BSA conformation to a more expanded phase following surface saturation [13]. When BSA surface density is high, conversion from the normal (N) form to the expanded (E) form results in the protein chain extending out from the surface, and thus should result in fewer contact points [13]. With fewer contact points, it is likely that the binding affinity would decrease. In this study, three different methods were tested to modify the
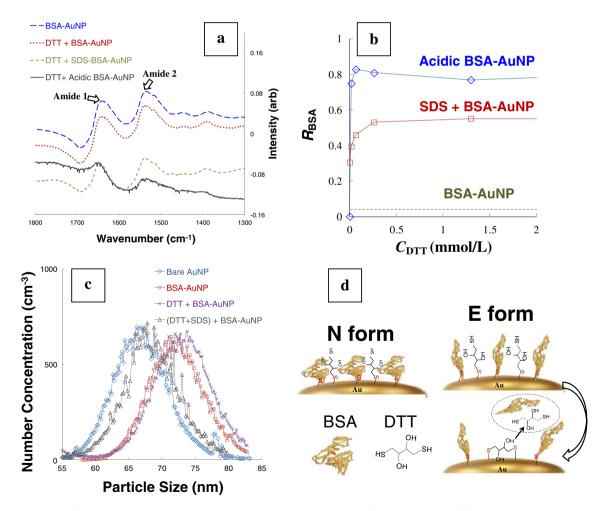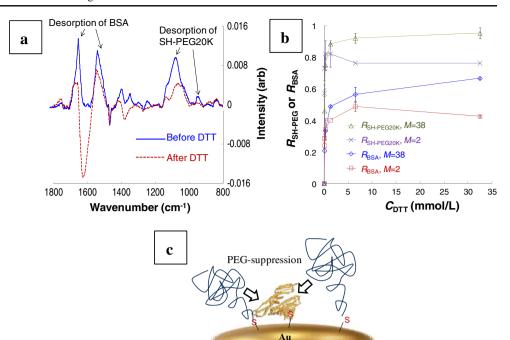

Fig. 3 Comparison of DTT displacement on BSA-conjugated AuNPs following different denaturization procedures. **a** ATR-FTIR. Spectra were collected after treatment at C_{DTT}=6.5 mmol/L followed by rinsing with DI water. Background: AuNPs in DI water. **b** Displacement ratio calculated from ATR-FTIR difference spectra. Background: BSA-conjugated AuNPs in DI water. **c** Particle size distributions measured by ES-DMA. **d** Cartoon depiction of DTT displacement in the presence of modified BSA conformation

Fig. 4 Characterization of DTT displacement on the SH-PEG/BSA–AuNP conjugates at pH 2 using ATR-FTIR. **a** IR absorbance spectra before and after DTT displacement. Background: AuNPs in DI water. **b** Displacement ratios of SH-PEG20K and BSA versus C_{DTT} for different M. **c** Cartoon depiction of the SH-PEG+BSA+AuNP system

adsorbed BSA conformation to obtain better detachment efficiency: (1) acidification (reducing the pH to 2) [13, 15], (2) addition of a denaturant (sodium dodecyl sulfate, or SDS) [15], and (3) thermal stress (by heating above 55 °C for 2 h) [3].

As shown in Fig. 3a, acidification (the first from the bottom, solid) and SDS treatment (the second from the bottom, short dash) resulted in a substantial decrease to the intensity of the amide II band as measured by ATR-FTIR, indicating that the denaturing process significantly improves the displacement efficiency of DTT in the case of BSA. Using the ATR-FTIR results, the BSA displacement efficiency R_{BSA} was calculated as a function of C_{DTT} (as shown in Fig. 3b); details for these calculations are provided in the ESM. Prior to altering the conformation, R_{BSA} is close to zero. However, after adjusting the pH to an acidic state (method 1), R_{BSA} increases significantly, with a maximum value of $R_{BSA}=82$ % at $C_{DTT}>1$ mmol/L. Similarly, after using the denaturant SDS (method 2) at $C_{SDS}=35$ mmol/L for 5 min and then water rinsing, R_{BSA} increases to ≈55 % Thus, in both cases, the prescribed method alters the BSA conformation towards its E-form, thereby decreasing its binding affinity and increasing its predisposition to DTT-induced desorption. In contrast,

thermal treatment was found to have a minimal impact on the BSA displacement ratio (i.e., R_{BSA} remained close to zero) over the temperature range studied.

Orthogonally, ES-DMA was used to measure $H_{t,DMA}$ (i.e., half of $\Delta d_{p,m}$) from which we calculate R_{BSA}. Figure 3c illustrates the particle size distribution of BSA-conjugated AuNPs before and after treatment with DTT. Before adding DTT, $H_{t,DMA}≈2.5$ nm with no increase in distribution width relative to the native (unconjugated) AuNPs, signifying formation of a uniform BSA layer and the absence of agglomeration. At neutral pH, $H_{t,DMA}$ increases slightly, confirming the previously observed poor displacement efficiency for DTT on BSA. However, after adding the denaturant SDS (method 2) and interacting at $C_{SDS}=3.2$ mmol/L, $H_{t,DMA}$ decreases to ≈0.8 nm ($R_{BSA}=92$ %), showing that BSA is more effectively displaced by DTT after denaturing the bound BSA (results for the acidification treatment were inconclusive due to flocculation during the sample preparation prior to ES-DMA analysis). DLS results also show a decrease in $H_{t,DLS}$ after adding DTT to both acidified and SDS-treated samples (see ESM). Overall, the results confirm that the displacement efficiency for DTT on BSA–AuNP can be improved when the conformation of BSA is modified from the compact N-form to the

Table 3 Summary of R_{BSA}, $R_{SH-PEG20K}$, $K_{d,BSA}$, and $K_{d,SH-PEG20K}$ results from ATR-FTIR

$C_{SH-PEG20K}/C_{BSA}$	$\sigma_{SH-PEG20K}/\sigma_{BSA}$	R_{BSA} (%)	$R_{SH-PEG20K}$ (%)	$K_{d,BSA}$ (L/mol)	$K_{d,SH-PEG20K}$ (L/mol)
0	0	82±8	N/A	$7.1×10^5$	N/A
2	1.07±0.18	49±3	82±8	$1.7×10^4$	$1.3×10^5$
38	0.95±0.11	57±5	92±3	$7.9×10^3$	$9.3×10^4$

more open and elongated E-form (at high adsorption densities); a depiction of this process is shown in Fig. 3d.

SH-PEG/BSA-conjugated AuNPs

In a recent study, ATR-FTIR was used to show that SH-PEG inhibits the *adsorption* of BSA on AuNPs; notably, the inhibition increases as M_m increases, indicating perhaps a stronger steric hindrance from higher-M_m SH-PEG [14]. Here, we investigate the *desorption* of SH-PEG and BSA from AuNPs as induced by DTT, and more specifically, if the presence of one ligand changes the desorption behavior of the other ligand. As noted in previous multiple ligand studies, dimensional characterization methods are not always conclusive as it is difficult to quantify both SH-PEG and BSA desorption based only on a change in average particle size [11, 14, 15]. Because of the distinguishable characteristic absorption bands associated with SH-PEG, BSA, and DTT, ATR-FTIR was used to characterize DTT displacement in the multi-ligand system. Two C_{SH-PEG}/C_{BSA} ratios (defined as M) were studied: $M=2$ and $M=38$ (only the results for SH-PEG20K are shown; SH-PEG with different M_m exhibited similar trends). Despite the large difference in concentration ratio, we found the adsorption ratio, $\sigma_{SH-PEG}/\sigma_{BSA}$, is close to unity in both cases, indicating that $\sigma_{SH-PEG}/\sigma_{BSA}$ is relatively constant in this concentration ratio range, but perhaps not at different *absolute* values for ligand concentrations. For instance, a possible reason for the $\sigma_{SH-PEG}/\sigma_{BSA}$ invariance is that SH-PEG20K and BSA are present in relatively large concentrations and have similar equilibrium binding constants (10^5 to 10^6 L/mol) [13, 14]. As shown in Fig. 4a, absorption bands signifying SH-PEG20K and BSA adsorption are observed after simultaneously introducing the two ligands to the AuNPs. Following SH-PEG/BSA conjugation, the pH was lowered (method 1 above), and DTT was subsequently added. Consequently, the intensities of the SH-PEG20K and BSA adsorption bands decrease, thereby increasing R_{BSA} and R_{SH-PEG}. Examining these results more closely, both R_{BSA} and R_{SH-PEG} increase as C_{DTT} increases at small C_{DTT}, but reaches maximum values at $C_{DTT}>6.5$ mmol/L, as shown in Fig. 4b.

The results for R_{BSA} and R_{SH-PEG} and the corresponding values for $K_{d,SH-PEG}$ and $K_{d,SH-PEG}$ are given in Table 3. In this C_{DTT} range, the maximum R_{BSA} is ≈50 to 60 %, smaller than the value without SH-PEG20K present (≈80 %). A possible explanation for the decrease in R_{BSA} could be related to an increase in BSA binding with the AuNP surface in the presence of SH-PEG20K conjugates; the SH-PEG20K could suppress the conformation of the BSA and thus induce more contact points between the BSA and the AuNP surface (as depicted in Fig. 4c). Consequently, $K_{d,BSA}$ also slightly decreases, from ≈7×10^5 to ≈10^4 L/mol. In contrast, the displacement efficacy of SH-PEG20K is relatively unchanged, or even slightly larger, in the presence of BSA; R_{SH-PEG} is ≈80 to

90 %, or close to the value without BSA (77 %, Table 2). As a result, $K_{d,SH-PEG}$ (≈10^5 L/mol) is an order of magnitude larger than $K_{d,BSA}$. The results indicate that DTT preferably displaces SH-PEG20K ligands over BSA due, presumably, to weaker binding of SH-PEG20K to the AuNP surface (single S–Au bond, little contribution from hydrophilic polymer chain). BSA, in contrast, has multiple potential binding sites (thiol, amine) and hydrophobic residues that, under a denatured conformation, could help stabilize the adsorbed state and provide resistance to DTT displacement.

Conclusions

Through a comprehensive study utilizing complementary measurement methods, we have advanced our understanding of the DTT displacement of ligands bound to AuNPs. We have quantified the displacement ratios for two different classes of functional ligands (i.e., BSA and SH-PEG) and have examined the role of molecular mass (for SH-PEG). The displacement ratio is strongly dependent on the individual ligand binding affinity to AuNPs and is less affected by steric hindrance (e.g., it is largely independent of M_m). The binding affinity of ligand conjugates may be affected by a number of factors, including the presence of neighboring ligands, surfactants, and pH conditions. Our results show that neither SH-PEG nor BSA can be completely removed from AuNPs by DTT treatment; BSA in particular shows a very low displacement efficiency at physiological pH. The displacement efficiency of BSA conjugates can be improved significantly through processes that affect the folding of the bound protein, such as pH reduction and addition of a denaturant. Our study provides a prototypical approach to improve the detach-and-analyze methodology and should be applicable to other types of nanoparticle-ligand systems. Future research should focus on the underlying mechanistic understanding of ligand detachment by DTT under relevant solution conditions and when multiple ligands are simultaneously or serially present. Additionally, the application of chemometric analysis may improve quantification of spectroscopic results in the future, and should be explored for the present application.

References

1. Paciotti GF, Myer L, Weinreich D, Goia D, Pavel N, McLaughlin RE, Tamarkin L (2004) Drug Deliv 11:169–183
2. Giljohann DA, Seferos DS, Daniel WL, Massich MD, Patel PC, Mirkin CA (2010) Angew Chem Int Edit 49:3280–3294

3. Mirkin CA, Hill HD (2006) Nat Protoc 1:324–336
4. Paciotti GF, Kingston DGI, Tamarkin L (2006) Drug Develop Res 67:47–54
5. McNeil SE, Hall JB, Dobrovolskaia MA, Patri AK (2007) Nanomedicine-UK 2:789–803
6. Pease LF, Tsai DH, Zangmeister RA, Zachariah MR, Tarlov MJ (2007) J Phys Chem C 111:17155–17157
7. Eck W, Craig G, Sigdel A, Ritter G, Old LJ, Tang L, Brennan MF, Allen PJ, Mason MD (2008) Acs Nano 2:2263–2272
8. Tsai DH, Zangmeister RA, Pease LF, Tarlov MJ, Zachariah MR (2008) Langmuir 24:8483–8490
9. Dobrovolskaia MA, Aggarwal P, Hall JB, McLeland CB, McNeil SE (2009) Adv Drug Deliver Rev 61:428–437
10. Dobrovolskaia MA, Patri AK, Zheng JW, Clogston JD, Ayub N, Aggarwal P, Neun BW, Hall JB, McNeil SE (2009) Nanomed-Nanotechnol 5:106–117
11. Tsai DH, DelRio FW, MacCuspie RI, Cho TJ, Zachariah MR, Hackley VA (2010) Langmuir 26:10325–10333
12. Tsai DH, Cho TJ, DelRio FW, Taurozzi J, Zachariah MR, Hackley VA (2011) J Am Chem Soc 133:8884–8887
13. Tsai DH, DelRio FW, Keene AM, Tyner KM, MacCuspie RI, Cho TJ, Zachariah MR, Hackley VA (2011) Langmuir 27:2464–2477
14. Tsai D-H, Davila-Morris M, DelRio FW, Guha S, Zachariah MR, Hackley VA (2011) Langmuir 27:9302–9313
15. Tsai D-H, Elzey S, DelRio FW, Keene AM, Tyner KM, Clogston JD, MacCuspie RI, Guha S, Zachariah MR, Hackley VA (2012) Nanoscale 4(10):3208
16. El-Sayed MA, Dreaden EC, Mackey MA, Huang XH, Kang B (2011) Chem Soc Rev 40:3391–3404
17. Mu CJ, LaVan DA, Langer RS, Zetter BR (2010) Acs Nano 4:1511–1520
18. Kanaras AG, Bartczak D, Muskens OL, Millar TM, Sanchez-Elsner T (2011) Nano Lett 11:1358–1363
19. Libutti SK, Paciotti GF, Byrnes AA, Alexander HR, Gannon WE, Walker M, Seidel GD, Yuldasheva N, Tamarkin L (2010) Clin Cancer Res 16:6139–6149
20. ClinicalTrials.gov, **2011**.
21. Hall JB, Dobrovolskaia MA, Patri AK, McNeil SE (2007) Nanomedicine-UK 2:789–803
22. Hurst SJ, Lytton-Jean AKR, Mirkin CA (2006) Anal Chem 78:8313–8318
23. MacDairmid AR, Gallagher MC, Banks JT (2003) J Phys Chem B 107:9789–9792
24. Creczynski-Pasa TB, Millone MAD, Munford ML, de Lima VR, Vieira TO, Benitez GA, Pasa AA, Salvarezza RC, Vela ME (2009) Phys Chem Chem Phys 11:1077–1084
25. Jokerst JV, Lobovkina T, Zare RN, Gambhir SS (2011) Nanomedicine-UK 6:715–728
26. *The identification of any commercial product or trade name does not imply endorsement or recommendation by the National Institute of Standards and Technology.*
27. Zhou L, Rai A, Piekiel N, Ma XF, Zachariah MR (2008) J Phys Chem C 112:16209–16218
28. Tsai DH, Pease LF, Zangmeister RA, Tarlov MJ, Zachariah MR (2009) Langmuir 25:140–146
29. Elzey S, Tsai D, Rabb S, Yu L, Winchester M, Hackley V (2012) Anal Bioanal Chem 403:145–149
30. Socrates G (1994) Infrared characteristic group frequencies. Wiley, New York
31. Woods DA, Petkov J, Bain CD (2011) J Phys Chem B 115:7353–7363
32. Carter DC, Ho JX (1994) Adv Protein Chem 45:153–203